

Non-equilibrium pathways between cluster morphologies in active phase separation: necking, rupture and cavitation

Liheng Yao (姚立衡),^{1,2} Michael E. Cates,¹ and Robert L. Jack^{1,3}

¹*DAMTP, Centre for Mathematical Sciences, University of Cambridge, Wilberforce Road, Cambridge CB3 0WA, United Kingdom*

²*Université Grenoble Alpes, CNRS, LIPhy, 38000 Grenoble, France*

³*Yusuf Hamied Department of Chemistry, University of Cambridge, Lensfield Road, Cambridge CB2 1EW, United Kingdom*

We investigate the dynamical pathways of a geometric phase transition in a two-dimensional active lattice gas undergoing motility-induced phase separation. The transition is between metastable morphologies of the liquid cluster: a system-spanning “slab” and a compact “droplet”. We generate trajectories of this transition in both directions using forward flux sampling. We find that the droplet-to-slab transition always follows a similar mechanism to its equilibrium counterpart, but the reverse (slab-to-droplet) transition depends on rare non-equilibrium fluctuations. At low Péclet numbers the equilibrium and non-equilibrium pathways compete, while at high Péclet numbers the equilibrium pathway is entirely suppressed, and the only allowed mechanism involves a large vapour bubble. We discuss the implications of these findings for active matter systems more generally.

I. INTRODUCTION

Active matter systems are driven away from equilibrium by continuous injection of energy at a microscopic level. Within this class, systems of self-propelled particles have been widely studied in recent years: they are tractable both analytically and numerically and reveal a range of interesting large-scale behaviour, including motility-induced phase separation (MIPS), where purely repulsive particles spontaneously separate into a dense liquid phase and a dilute vapor [1–4]. This phenomenon shares many features with liquid-vapor phase separation at equilibrium, but there are also important differences. For this reason, MIPS phenomenology is a natural place to test and develop methods for non-equilibrium systems, and to compare with equilibrium cases.

Phase-separated states are also natural settings to investigate the “controllability” of many-body physical systems. For example, the morphology of liquid and vapor domains and the wetting behavior at interfaces can both be engineered via surface tensions between the liquid, vapor, and solid. It may also be desirable to control the transitions between different metastable states, such as the slab and droplet morphologies of a liquid domain in a phase-separated system with periodic boundaries. Here, the slab morphology involves a liquid domain that crosses the periodic boundaries, and has flat interfaces; the droplet morphology has a circular or spherical domain with curved interfaces. (The free energy difference between these states depends on the overall density.) In general, the control of such transitions is intrinsically linked with the mechanism of (often rare) spontaneous transitions via a general connection between optimal-control theory and large deviation theory [5–10]. The central idea is that the minimal forces required to induce a dynamical transition are those that realise the mechanism by which it would happen spontaneously (but rarely).

In fact, characterisation of the transition mechanism between liquid slab and droplet states is already a challenging problem in equilibrium liquid-vapour systems [11, 12]. Such rare events are often studied in the context of dewetting and capillary condensation in systems confined between hydrophobic surfaces [13–18]. For the idealised case of the 2d Ising lattice gas with periodic boundaries, it was found by Moritz *et al.* [12] that two reaction coordinates are required to characterise the transition, with one quantifying the neck that forms in the transition state, and the other quantifying the roundness of the cluster. These co-ordinates have quite different characteristic time scales, so the mechanism involves a relatively slow change of cluster shape, while formation (or breakage) of the neck is much faster. The surface tension (and its curvature dependence [19, 20]) are obviously relevant for this rate, but differing time scales for the two co-ordinates also influence the mechanism, through the presence of two distinct mobilities [12].

This work presents a numerical characterisation of spontaneous transitions between liquid slab and droplet states in an active lattice gas (ALG) that was previously shown to exhibit MIPS [21]. This is achieved by forward flux sampling (FFS), which enables efficient characterisation of such rare events [22–24]. Compared with the equilibrium case, the situation is more complicated for several reasons. Firstly, interfacial phenomena in systems undergoing MIPS are significantly different from their equilibrium counterparts, with some effective measures of surface tension giving negative values in certain parameter ranges [25–28]. Moreover, such systems can exhibit bubbly phase separation, where stable bubbles grow within the liquid cluster until they are expelled into the surrounding vapor [21, 27, 29, 30], a phenomenon without any equilibrium equivalent. More exotic interfacial phenomena such as active foam states have also been found [31], and there are also interesting analogies with wetting when the liquid phase comes into contact with solid surfaces [32–36]. Understanding and control-

ling transitions in MIPS systems offers a route towards control of these states.

By using FFS, we are able to collect ensembles of trajectories that make transitions between slab and droplet geometries in the ALG: these are called *reactive trajectories*. This application rests on the fact that (i) FFS is applicable to non-equilibrium systems (the ALG violates detailed balance); and (ii) FFS does not require knowledge of an accurate reaction coordinate [24]. Based on these trajectories, we analyse the transition mechanism.

To briefly summarise the main results, recall that the Péclet number (Pe) quantifies the strength of the particles' self-propulsion. We consider four state points, two of which have lower values of Pe, and two have higher values. In all cases, we find that the transition mechanism from droplet to slab resembles that found in [12] for the equilibrium case (Ising model). It is characterised by slow dynamics for droplet shape ("roundness"), both before and after the formation of a neck (which changes the topology of the liquid domain). On the other hand, we find that transitions from slab to droplet take place by distinct mechanisms that do not correspond to time-reversed transitions from droplet to slab. This is a non-equilibrium effect, due to the broken time-reversal symmetry of the steady state. We find that the equilibrium-like slab-to-droplet mechanism resembles ductile failure of an amorphous material under mechanical load, including a necking effect [37–40]. The non-equilibrium mechanisms instead resemble failure by brittle rupture, mediated by voids inside the dense phase and cavitation effects [39, 41–43]. This leads to a qualitative analogy between fracture mechanisms under external stress, and spontaneous transitions in active systems without external loading.

In what follows, we present our model and computational methods in Sec. II, report our findings in Sec. III, and conclude with a discussion in Sec. IV.

II. MODEL AND METHODS

A. Model definition

We use the active lattice gas (ALG) introduced in [21], where a 2-dimensional lattice of size L^2 and lattice spacing a is populated with $N = \rho(L/a)^2$ particles. Each lattice site can contain at most 1 particle, and the orientation vector of particle k is $\mathbf{u}_k = (\cos \theta_k, \sin \theta_k)$. This orientation fluctuates over time with a diffusion coefficient D_O . Particle k jumps from site i to an unoccupied neighboring site j with rate

$$W_{ij} = \frac{2D_E/a^2}{1 + \exp[-av_0(\mathbf{u}_k \cdot \mathbf{e}_{ij})/D_E]}, \quad (1)$$

where \mathbf{e}_{ij} is a vector that points from site i to site j , D_E is the translational diffusion constant, and v_0 is the persistence. The rate expression (1) is chosen so that (i)

State	v_0	D_E	l_p	Pe	ρ
A1	100	10	20.0	6.32	0.38
A2	55	50	50.1	7.08	0.45
B1	130	30	58.4	10.7	0.38
B2	100	50	76.2	10.8	0.41

TABLE I. The four state points considered in this work. We have set $a = 1$ and $D_O = 1$.

the model converges to that of Mason *et al.* [44] in the limit $av_0 \ll D_E$, for which an exact hydrodynamic limit has been derived, and (ii) the transition rates satisfy local detailed balance (see e.g. [45]).

The translational moves are implemented through the Gillespie algorithm [46, 47]: the total rate of all allowed transitions $R = \sum W_{ij}$ is computed, and one of the events is picked to happen with probability W_{ij}/R , using a binary search tree. The time is then advanced by $1/R$, and the affected rates W_{ij} are updated. This process is repeated until the time has been advanced by a total increment δt , chosen such that $a^2 D_E^{-1} \ll \delta t \ll D_O^{-1}$. After each such increment, the orientation of each particle is updated by an independent Gaussian random variable $\delta \theta_k \sim \mathcal{N}(0, \sqrt{2D_O \delta t})$, in order to implement the rotational diffusion.

The lengthscales that control the behavior of this model are the diffusive length $l_D = \sqrt{D_E/D_O}$, and the persistence length l_p (see below), which gives the distance traveled by an isolated particle within its orientational diffusion timescale D_O^{-1} . The dimensionless Péclet number $\text{Pe} = l_p/l_D$ then measures the strength of the activity in the system, and therefore its distance from equilibrium. As discussed in [21], the non-linear dependence of W_{ij} on v_0 means that l_p and Pe are given by

$$l_p = \frac{2D_E}{aD_O} \tanh\left(\frac{av_0}{2D_E}\right), \quad \text{Pe} = \frac{2}{a} \sqrt{\frac{D_E}{D_O}} \tanh\left(\frac{av_0}{2D_E}\right). \quad (2)$$

For the purpose of this work, we fix the units of time and space by setting $D_O = 1$ and $a = 1$.

As shown in [21], this model exhibits MIPS and bubbly phase separation for a range of parameter choices. We will show results at four state points, which are listed in Table I. Two of these (A1, A2) have relatively low Péclet numbers, but with different diffusive lengths and hence also different persistence lengths; the other two state points (B1, B2) have larger Pe. For all these parameters, the steady state of the system is phase coexistence between a dense liquid cluster and a dilute vapor. The densities are chosen such that the liquid cluster is (meta)stable in both a system-spanning slab geometry and a compact droplet geometry, with rare transitions between these geometries. All results are for system size $L = 100$. The spontaneous formation of bubbles in the liquid phase depends significantly on system size [21]: for state points B1,B2 and these system sizes, *typical* configurations do not have any bubbles; for A1,A2 some bubbles are visible, see below (Figs. 3 and 6).

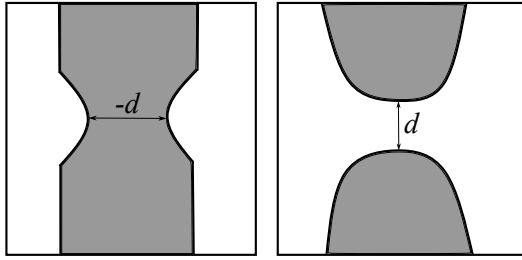


FIG. 1. Illustration showing the definition of the reaction coordinate d , when the system is in the slab (left) or droplet (right) geometry.

B. Order parameters

In modern theories of rare events (see e.g. [48]), trajectories between metastable states are projected onto one or more order parameters, which are observable quantities that contain information about the mechanism of the transition, and in some cases can be used to calculate transition rates. For transitions with more than one order parameter, a simple signature of irreversibility is that differences appear between forward and backward trajectories when projected onto the order parameters.

Our choice of order parameters follows Ref. [12], which studied the transition between slab and droplet geometries in the $2d$ Ising model under Kawasaki dynamics [49]. The allowed MC moves in that case are particle jumps to nearest unoccupied neighbouring sites, with rates obeying detailed balance with respect to the Ising interaction at temperature T . They used two order parameters to construct a *reaction coordinate* for the transition, which allows the transition rate to be related to a free-energy barrier.

Our first order parameter, denoted d , is illustrated schematically in Fig. 1: it measures either the width of a neck that forms in the slab before breaking, or the width of the channel that opens up after breaking. The two situations are differentiated by the sign of d , which is positive in the droplet state and negative in the slab state. We note that our definition of d is slightly different from that in [12], as we only measure the (integer-valued) distance in the x or y directions, while the authors of [12] measure the absolute distance (that may not necessarily be in the lattice directions), and add in a constant offset. Our definition makes for easier computational implementation without any significant effect on the physics.

The second order parameter, denoted s , measures the “roundness” of the liquid cluster with larger values in the droplet state, and smaller ones in the slab state. Consider the occupancy σ_{xy} for the lattice site at position (x, y) , which takes the value 1 if the site is occupied and 0 otherwise. We denote the components of its Fourier transform as $\tilde{\sigma}_{pq}$ [corresponding to wavevector $2\pi a(p, q)/L$ for inte-

gers p, q] and calculate

$$s = \min \left(\frac{|\tilde{\sigma}_{01}|}{|\tilde{\sigma}_{10}|}, \frac{|\tilde{\sigma}_{10}|}{|\tilde{\sigma}_{01}|} \right). \quad (3)$$

Note that a slab oriented along the y -axis has large $\tilde{\sigma}_{10}$ and small $\tilde{\sigma}_{01}$; the opposite is true for a slab oriented along the x -axis: these both have small s . By contrast the a circular droplet has $|\tilde{\sigma}_{10}| \approx |\tilde{\sigma}_{01}|$ so $s \approx 1$.

Both coordinates quantify progress along any transition between the two geometries. However, these transitions are controlled by rare events that are impractical to simulate using brute-force methods. Instead we use a rare-event sampling method, as described next.

C. Forward flux sampling

To generate rare trajectories between cluster geometries, we use forward flux sampling (FFS) [24]. Note that this algorithm does not require the system to be in equilibrium; nor does it require accurate knowledge of the reaction coordinate. However, sampling efficiency is greatly improved if one does have a good approximation of the reaction co-ordinate [24], which can make the difference between tractable and intractable calculations. The algorithm foliates reactive trajectories along a chosen coordinate, which we choose to be the roundness measure s . This choice has various benefits: (a) the value of s varies smoothly between 0 and 1, irrespective of model parameter choices, and (b) s is a slow coordinate compared to d , and unlike d , does not undergo large fluctuations during the transition.

To perform FFS, we place a set of milestones s_i with $i = 0, 1, 2, \dots, m$ in increasing order between 0 and 1. The interfaces are defined such that configurations considered to be in the slab basin have $s < s_0$ and those considered to be in the droplet basin have $s \geq s_m$. We describe the method of generating an ensemble of trajectories from the slab state to the droplet. (The reverse transition is sampled analogously.) The algorithm depends on a parameter N_c , which is the number of reactive trajectories that are sampled. Not all these trajectories are independent, see below. The method is guaranteed to provide accurate results in the limit of large N_c ; the convergence of this limit is discussed below.

The first part of the algorithm samples a set of N_c initial conditions for the trajectories. These have a roundness parameter s between s_0 and s_1 . They are obtained by preparing a system in the metastable slab state, and running a long dynamical trajectory. We collect configurations whenever s increases from $s < s_0$ to $s \geq s_0$, until we have obtained N_c in total. The reactive flux I_0 through the initial interface is given by the number of collected configurations N_c divided by the total duration of this trajectory.

From here, the algorithm proceeds one milestone at a time. Starting from the ensemble at $i = 0$ (which has $s_i < s < s_{i+1}$), we select a random configuration and

evolve it until its roundness either reaches s_{i+1} or returns to s_0 . This procedure is repeated until N_c configurations have been obtained with $s_i < s < s_{i+1}$: these form the ensemble at milestone i . Increasing i stepwise, we eventually reach the final milestone ($i = m$), at which point N_c reactive trajectories have been obtained.

The probability that a configuration collected at s_i reaches s_{i+1} before it returns to s_0 can be estimated at each interface, and is denoted $P(s_{i+1}|s_i)$. As configurations with $s > s_m$ are considered to be in the product basin with probability 1, the transition rate is given by

$$I_{\text{FFS}} = I_0 \prod_{i=0}^{m-1} P(s_{i+1}|s_i) . \quad (4)$$

In the limit of large N_c , this transition rate converges to the physical transition rate.

In our simulations, we place $m = 18$ milestones between $s = 0.08$ and 0.98 , with an even spacing of 0.05. The placement of the initial interfaces allows crossings of the initial interface to be reasonably spaced apart in time, so that the configurations collected there are not highly correlated. However, our choice also allows crossings to be frequent enough for a large number of configurations to be collected. The spacings between milestones are wide enough that trajectories do not “overshoot” (crossing more than one milestone at a time), but narrow enough to still be computationally efficient.

III. RESULTS

We perform FFS for transitions in both the slab-to-droplet and droplet-to-slab directions, for a lattice of size $L = 100$, at densities where both slab and droplet geometries are (meta)stable (recall Tab. I). For each configuration collected at the milestones, we measure the values of s and d (the measured s values are all very close to the milestone values, as expected), allowing us to reconstruct reactive trajectories. For each FFS run, we can then average the s and d values at each milestone, yielding the averaged reactive pathway.

We present results for the four state points shown in Tab. I which we separate according to their Péclet numbers. For the smaller Pe (parameters A1,A2) our results in Sec. III A are sufficient to establish significant differences between slab-to-droplet and droplet-to-slab transitions. We find in particular a distinct non-equilibrium mechanism for the slab-to-droplet case, where the slab breaks at a relatively small value of the roundness parameter, which is coupled with density fluctuations (transient bubbles) inside the slab. We also analyse convergence of the FFS method. For the larger Pe, the calculations are much more challenging: we present clear numerical evidence in Sec. III B for a non-equilibrium slab-to-droplet transition mediated by a large bubble within the slab. However, the quantitative results (e.g. transition rates) in this case are subject to considerable uncertainty, due to the high computational cost of sampling.

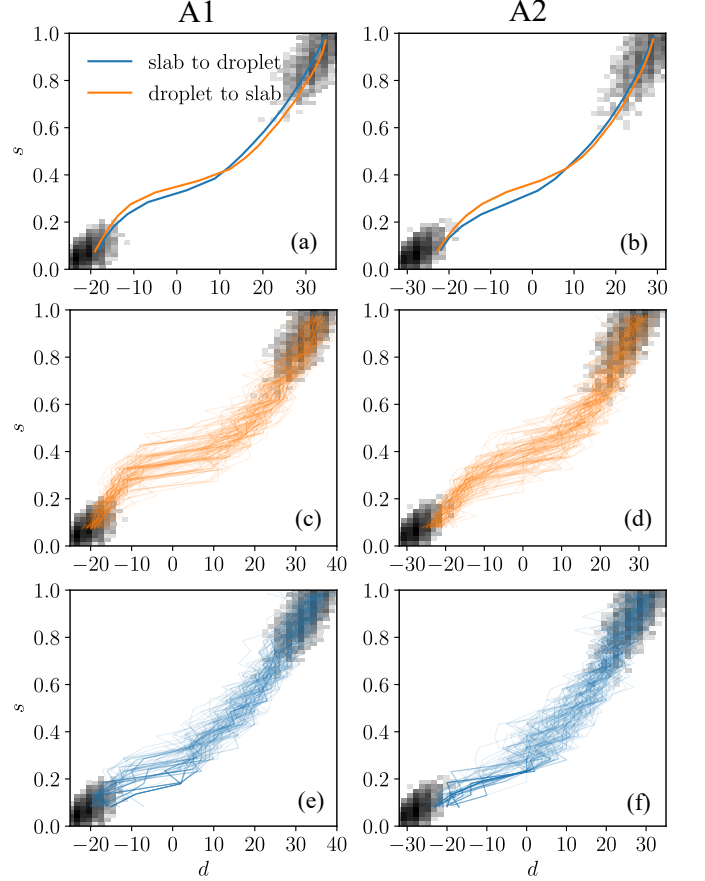


FIG. 2. (a,b) Average transition trajectories of parameters A1 (left column) and A2 (right column). (c,d) 100 sample trajectories of the droplet to slab transition for each parameter set. (e,f) 100 sample trajectories of the slab to droplet transition. The shadings indicate the probability distributions within the metastable basins, obtained by direct sampling. All trajectories are obtained using FFS runs with $N_c = 16000$.

A. Lower Péclet numbers

1. Pathways

We first consider parameters A1 and A2 in Table I, which have $\text{Pe} \approx 6.3, 7.1$, close to the onset of MIPS, which occurs between $\text{Pe} = 5$ and $\text{Pe} = 6$ for the densities we consider. We show the averaged transition pathways and 100 individual trajectories (selected at random from all collected trajectories) in Fig. 2. Some snapshots of the configurations along typical reactive trajectories in Fig. 3. For the individual trajectories shown in Fig. 2(c-f), we note that the branching inherent in FFS means that different trajectories may coincide with each other during the early parts of the transition: these appear as heavier lines in the Figure (we return to this point below). The FFS estimates of transition rates from slab-to-droplet and droplet-to-slab transitions are 4×10^{-9} and 9×10^{-9} for parameters A1, and 2×10^{-9} and 6×10^{-9} for parameters A2. The ratio of these rates provides an

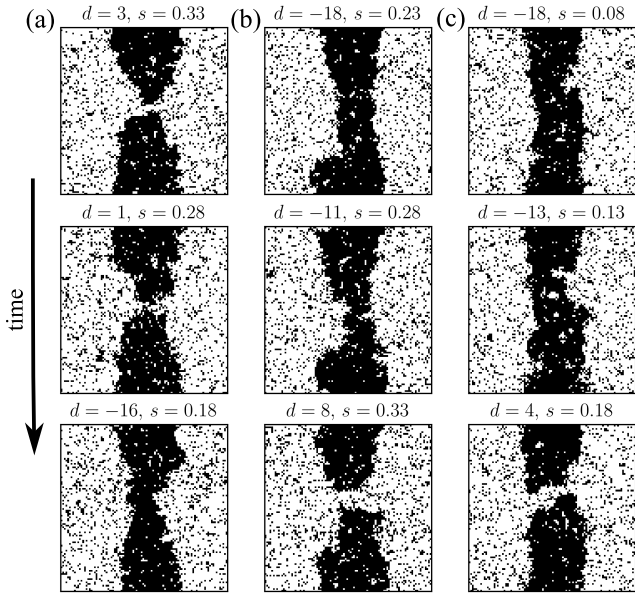


FIG. 3. Time-ordered snapshots taken from simulations of parameters A1, showing trajectories of (a) the formation of a slab from a droplet, (b,c) Two trajectories showing the slab-to-droplet transition showing an equilibrium-like mechanism (column b) and a non-equilibrium one (column c).

estimate of the relative probabilities of slab and droplet, showing that for both parameters the droplet state is 2 to 3 times more probable. For an equilibrium system, the free energy of the droplet increases with respect to the slab upon increasing density, due to surface tension. As a result, increasing the density makes the slab state more likely. We observe the same trend in the ALG, see Appendix B. This is in agreement with the previous result [21] that this ALG has a positive surface tension in the sense of capillary wave theory.

The droplet-to-slab transition is illustrated in Fig. 2(c,d) and Fig. 3(a). We find that the droplet gradually elongates its shape to leave a narrow channel of vapour; then it connects quickly across the channel, before relaxing to a stable (“straight”) slab geometry. The “fast connections” appear as the almost-horizontal segments in the individual trajectories shown in Fig. 2(c,d), showing a sharp changes in d with little change in s . We show time-ordered snapshots of the system just before and after the connection in Fig. 3(c). This is the same mechanism that was found for the 2d Ising model [12].

On the other hand, Fig. 2 shows that the mechanism for slab-to-droplet transitions in the ALG is not the reverse of the droplet-to-slab transition. This is a non-equilibrium feature: it is different from the Ising case where time-reversal symmetry (detailed balance) means that the averaged trajectories necessarily trace the same path, in opposite directions. In fact we find considerable diversity in the trajectories from slab to droplet, with two different examples shown in Fig. 3(b,c). We observe that

Fig. 3(b) qualitatively resembles the equilibrium pathway, which is also similar to the time-reversal of Fig. 3(a). However, inspection of Fig. 2(e) and (f), shows that this equilibrium-like pathway is in fact outweighed by trajectories where d increases suddenly while $s \lesssim 0.2$ is still small, within the range of fluctuations of the metastable slab.

An example of this process can be seen in Fig. 3(c). One sees that an indentation forms in the surface of the slab, which then connects with transient bubbles inside the slab, to form a channel of vapor. In equilibrium systems, this dent-like defect is likely to be quickly healed by surface tension, so trajectories involving this configuration are unlikely to carry significant weight in the ensemble of reactive trajectories. The existence of such a non-equilibrium transition mechanism is an example of the rich physical behaviour associated with motility-induced phase separation: many features of these systems resemble liquid-vapour coexistence at equilibrium, but signatures of the non-equilibrium behaviour are becoming increasingly clear [27, 29, 31, 32, 34, 35, 50]. These results may be compared with brittle (rupture) and ductile (necking) behaviour in the breakage of soft materials under external loading, see for example Fig. 5 of [39].

2. FFS convergence and physical discussion

As discussed in Sec. II C, the FFS algorithm samples representative reactive trajectories if N_c is sufficiently large [24]. However, convergence of this limit is not simple to achieve in practice [24, 51]. In general one expects better performance if the co-ordinate used to define the milestones is a good reaction co-ordinate for the transition of interest.

To investigate convergence, Fig. 4(a) shows averaged reactive trajectories for various N_c for parameters A2. Each curve comes from a single (representative) run of the FFS algorithm, which yields N_c reactive trajectories. Then s and d are averaged over the ensembles at each milestone. For the slab to droplet direction, there are significant run-to-run fluctuations of these averaged trajectories for $N_c \leq 8000$, but the results for the largest $N_c = 16000$ are robust. This slow convergence indicates that s is not a good reaction co-ordinate in this direction: it does not capture the bubbles that form inside the slab, which are implicated in the non-equilibrium mechanism.

Another way to see this effect is to measure the effective sample size for the reactive trajectories obtained from FFS. This quantity, defined in Appendix A, measures how many configurations from the first milestone contribute significantly to the sampled ensemble of reactive trajectories. It may be viewed as an approximation to the number of independent initial configurations that contribute to the sampled trajectories. For large N_c , it should grow linearly with N_c .

Results are shown in Fig. 4(b,c). The results for the droplet-to-slab transition indicate that the FFS is con-

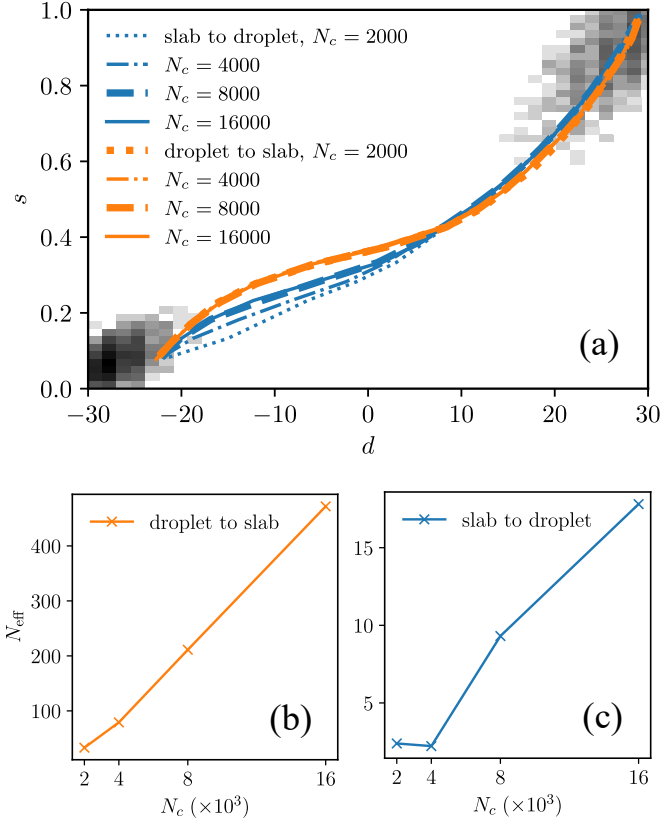


FIG. 4. (a) Averaged reactive trajectories for parameters A2 with various values of N_c . The shaded densities indicate probability distributions within of the metastable basins. (b), (c) The effective sample size at the initial milestone N_{eff} plotted against N_c .

verged, with hundreds of independent trajectories obtained from each run. However, the effective sample sizes N_{eff} are significantly smaller for the slab-to-droplet transition, which has $N_{\text{eff}} < 5$ for $N_c \leq 4000$. This indicates that the sampled trajectories are highly correlated, which explains the significant sample-to-sample fluctuations in this regime. The relatively poor performance in this case indicates that the roundness s is not a perfect reaction co-ordinate. In particular, it is not sensitive to small bubbles in the slab, which do affect the transition. Nevertheless, results for the largest values of N_c are consistent with linear growth of N_{eff} , and the FFS run yields many independent trajectories. The results of Fig. 4(a) also indicate convergence to two distinct averaged pathways, which are robust results of our calculations.

B. High Péclet numbers

We now show results for higher Péclet numbers of around 10.7: these are parameters B1 and B2 of Tab. I. The FFS calculations in this case are more computationally expensive compared to the lower Pe (see below for a discussion), so all results of this Subsection have

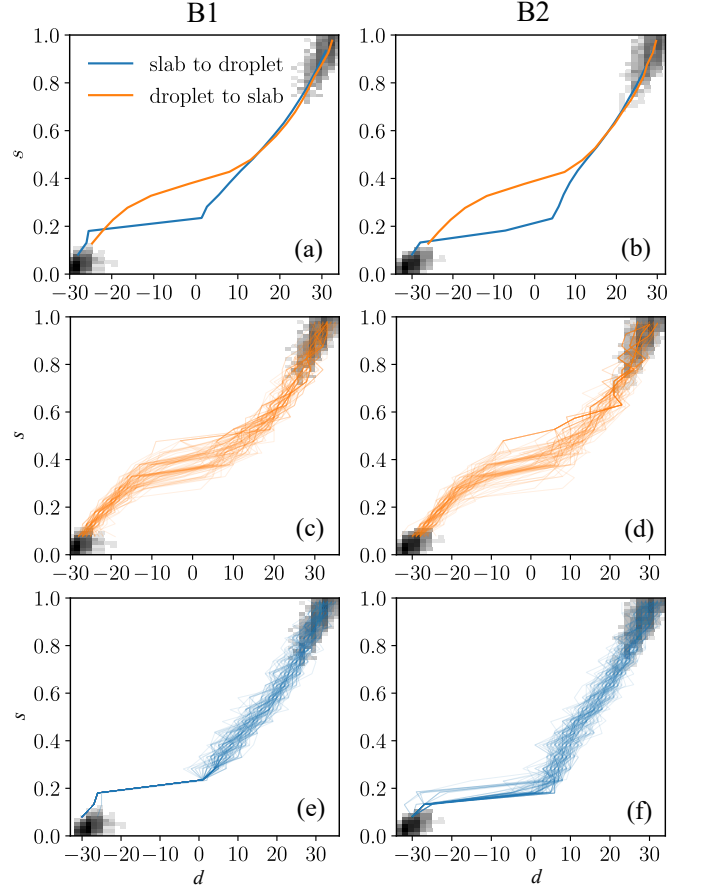


FIG. 5. Top to bottom: average transition trajectories of parameters (a) B1 and (b) B2; 100 sample trajectories of the droplet to slab transition for (c) B1 and (d) B2; 100 sample trajectories of the slab to droplet transition for (e) B1 and (f) B2. The density plots indicate the locations of the metastable basins. All trajectories are obtained using FFS runs with $N_c = 2000$.

$N_c = 2000$.

Again, we show the averaged transition pathways and 100 randomly selected trajectories in Fig. 5, and some snapshots of the configurations along typical reactive trajectories in Fig. 6. Despite the higher Péclet numbers, the droplet-to-slab transition is again equilibrium-like, as illustrated in the trajectories in Fig. 5(c,d) and Fig. 6(a).

However, the slab-to-droplet transition takes place by a different mechanism: for the results of Fig. 6, *all* the collected slab-to-droplet trajectories are observed to contain a large bubble at the initial milestone, from which a rupture develops through the slab. We show an example of this process in Fig. 6(b), it is reminiscent of the role of cavitation in the failure of metallic glasses, see for example [42, 52]. In the ALG at these high Péclet numbers, a flat interface is extremely stable, and shape fluctuations are strongly suppressed. As a result, slab rupture shows up in the d - s plane as a sudden increase in d with little change in s , as seen in Fig. 5(e) and (f). One sees from Fig. 5(a,b) that the forward and reverse transitions have

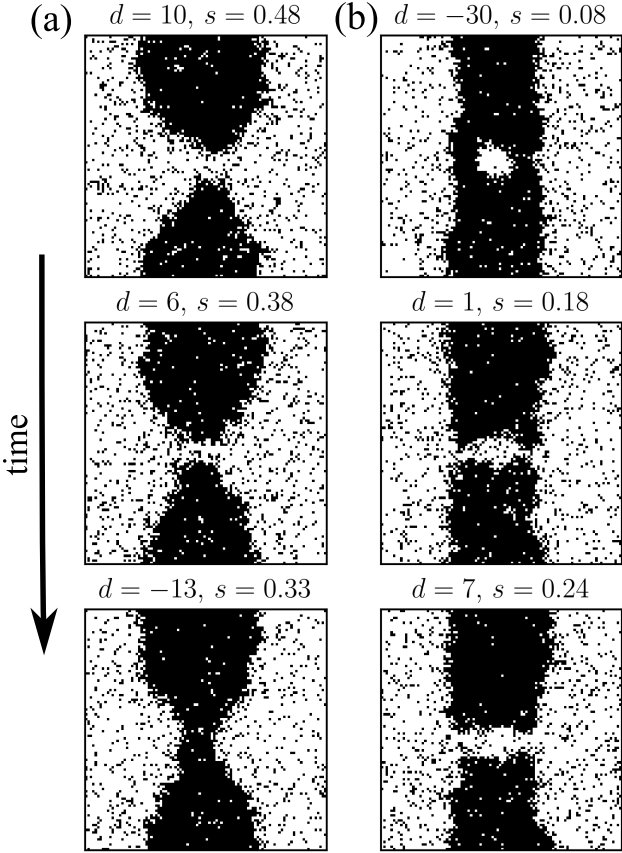


FIG. 6. Time-ordered snapshots taken from simulations of parameters B2, showing typical trajectories of (a) the breakdown of a slab into a droplet, and (b) the formation of a slab from a droplet.

very different mechanisms.

The non-equilibrium transition mechanism from slab to droplet at high Pe causes poor FFS convergence since the milestones are defined in terms of a poor reaction coordinate [24]. For each of the FFS calculations from slab-to-droplet in Fig. 5, all the reactive trajectories originate from just two initial configurations. That is, bubbles only appear in approximately one in a thousand of the configurations at milestone zero, because such configurations are not selected by the roundness parameter s . However, these few configurations will go on to completely dominate the final ensemble of reactive trajectories. As a result, at the second and third milestones the algorithm spends a large amount of time firing trajectories from non-bubbly configurations that nearly always return to the initial (slab) state.

This means that the effective sample sizes N_{eff} for both these calculations are between 1 and 2: such small numbers indicate that the FFS calculations are not fully converged. However, the observation of a bubble-mediated transition is reminiscent of the non-equilibrium mechanism found at smaller Pe (this was observed indepen-

dently for both parameter sets B1 and B2), suggesting that this behavior is likely to be generic. We also stress that since the FFS co-ordinate s favours equilibrium-like necking, the complete suppression of this mechanism in favour of bubble-mediated rupture strongly suggests that the latter will be the dominant pathway in spontaneous transitions. The existence of such mechanisms (for all state points considered) is the main physical result of this work. A useful direction for future research would be to develop order parameters that are sensitive to bubbles inside the slab, in order to improve the FFS convergence.

IV. DISCUSSION AND OUTLOOK

We have presented numerical results for the transition pathways between slab and droplet morphologies in an ALG undergoing MIPS. The natural comparison is with the work of Moritz *et al.* [12], which analysed the corresponding transitions in an equilibrium lattice gas with Ising interactions. We have emphasized that for the active system, the slab-to-droplet and droplet-to-slab transitions generically occur by different mechanisms, because time-reversal symmetry is explicitly broken, via the lack of detailed balance in the underlying dynamics.

For the droplet-to-slab transition, our results are qualitatively similar to the equilibrium case, as follows. The “roundness” co-ordinate s tends to evolve slowly since it requires mass transport over large (hydrodynamic) length scales; starting from a round droplet, s decreases from a value close to 1 as the droplet becomes increasingly elongated; the periodic boundaries mean that at some point the rapid formation of a neck becomes favourable and the order parameter d changes sign, signalling a change in topology from droplet to slab. After this, the roundness s continues to decrease until one reaches a uniform slab with flat interfaces.

As already noted, the slab-to-droplet transition does not generically look like a reversed version of the droplet-to-slab transition. For the lower values of Pe considered here (between 6.3 and 7.1), the change of topology from slab to droplet occurs on average at a smaller value of the roundness s [Fig. 3(a,b)]. Fig. 3 illustrates how an indentation in a flat slab can combine with vapour domains in its interior, with the result that the slab breaks by a sudden localised process. After this change – which occurs at small s – the resulting liquid domain gradually recovers the circular shape of a droplet ($s \approx 1$). For the larger Pe, the situation is different again, in that a vapour bubble nucleates inside the slab (Fig. 6(b)), which triggers the transition to the droplet. This again leads to a topology change at a relatively small value of s , compared to the (equilibrium-like) droplet-to-slab transition.

There are several possible routes towards a more detailed understanding of these transition pathways in MIPS. For further numerical work on this model, we expect the most fruitful direction to be development of new order parameters that can capture the reaction coordi-

nates: this would improve the efficiency of the FFS algorithm so that more data would be available, and characterisation of a good reaction co-ordinate would also yield extra insight into the transition. Other options would be to work on a fluctuating hydrodynamics description of a similar ALG, similar to [44], which would allow numerical calculations at continuum level. Alternatively one might work on field-theoretic models such as active model B+ [27, 53]. Comparison of these different MIPS systems would clarify which of the current results are generic and which are unique to the specific model considered here.

Finally, we note that the role of vapour “bubbles” inside the liquid is consistent with their presence in other aspects of active-matter physics including bubbly phase separation [27, 29, 30], which has also been observed previously in the typical behaviour of this ALG model [21]. The results of this work emphasize that even if the typical behaviour of phase separated states does not exhibit bubbles, rare events in such systems may still be mediated by bubbly mechanisms. (We also recall that the observation of bubbles depends significantly on system size in the ALG [21] and elsewhere [29], so it would be interesting to explore in more detail the system-size dependence of this mechanism.) There has been recent progress understanding nucleation in MIPS states [54]; results for that case might help to quantify the probability of the mechanism shown in Fig. 6, and to test whether it also appears in field-theoretic models such as active model B+ [27].

Overall, our results highlight the importance of non-equilibrium fluctuations such as persistent bubbles in phase transitions in active phase-separated systems. These fluctuations may fundamentally change the mechanisms of the transitions of interest, which are controlled by reaction co-ordinates that are different from the equilibrium case. Identifying effective non-equilibrium order parameters that can be used to quantify reactive trajectories then becomes important, because choosing a good order parameter greatly improves the efficiency of rare events sampling algorithms such as FFS.

ACKNOWLEDGMENTS

We thank the EPSRC for support through grant EP/Z534766/1.

Appendix A: Effective sample size

The branching nature of the FFS algorithm means that only a subset of the initial conditions (from milestone zero) contributes to the final ensemble of sampled trajectories. However, sampled trajectories that share the same initial condition are obviously not independent. (On the other hand, it is expected that trajectories from different initial conditions should be independent, as long as the harvesting of initial conditions is not correlated.) It is useful to quantify the effective sample size associated

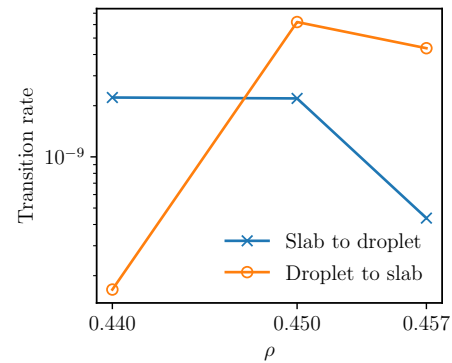


FIG. 7. Estimated transition rate as a function of density, for parameters A2.

with this branching, which is achieved by drawing on standard statistical methods [55], as follows.

For the k th initial configuration, we write w_k as the number of configurations collected at the final interface that stem from this initial configuration. The effective sample size is then defined as

$$N_{\text{eff}} = \frac{\left(\sum_{k=1}^{N_c} w_k\right)^2}{\sum_{k=1}^{N_c} w_k^2}. \quad (\text{A1})$$

Clearly, if one trajectory is sampled from each initial configuration, then $N_{\text{eff}} = N_c$. On the other hand, if just one initial condition is the source for all trajectories, then $N_{\text{eff}} = 1$. A larger N_{eff} indicates that more initial conditions are represented in the sampled ensemble of reactive trajectories.

Appendix B: Density dependence of the transition rate

For parameter set A2, we varied the density of the system, to further characterise the transitions. The mechanisms for droplet-to-slab and slab-to-droplet transitions were found to be very similar to the results presented in Figs. 2 and 3. In Fig. 7 we show the estimated transition rates as a function of density. These results are subject to significant statistical uncertainty but the trends are consistent with physical expectations. That is, increasing density reduces the rate for the slab-to-droplet transition, because the slab is thicker, and is therefore less likely to form a suitable neck or indentation in order to transform to the droplet. On the other hand, higher density increases the rate of transformation from droplet-to-slab, because the larger droplet requires less deformation in order to cross the periodic boundaries and form a slab. These are the same trends found in equilibrium systems.

The ratio of slab-to-droplet and droplet-to-slab transitions gives the ratio of the probabilities of the two states, within the steady state. The trends indicate that the slab

becomes more probable as the density increases. This effect is also consistent with the equilibrium case, where the interfacial free energy of the slab is $2\gamma L$ (with γ being the surface tension) while the interfacial free energy of the droplet is $2\pi\gamma R$ where R is the droplet radius. On increasing the density at fixed system size L , the droplet free energy increases (larger R) but the slab remains the

same. Hence the slab becomes more probable, as expected. (Eventually the density becomes so high that a circular liquid droplet cannot fit in the simulation box. At this point the droplet state no longer exists; one may consider instead a liquid that surrounds a single macroscopic vapour bubble.)

[1] J. Tailleur and M. E. Cates, Statistical Mechanics of Interacting Run-and-Tumble Bacteria, *Phys. Rev. Lett.* **100**, 218103 (2008).

[2] Y. Fily and M. C. Marchetti, Athermal Phase Separation of Self-Propelled Particles with No Alignment, *Phys. Rev. Lett.* **108**, 235702 (2012).

[3] G. S. Redner, M. F. Hagan, and A. Baskaran, Structure and Dynamics of a Phase-Separating Active Colloidal Fluid, *Phys. Rev. Lett.* **110**, 055701 (2013).

[4] M. E. Cates and C. Nardini, Active phase separation: new phenomenology from non-equilibrium physics, *Rep. Prog. Phys.* **88**, 056601 (2025).

[5] Dupuis and Ellis, *A weak convergence approach to the theory of large deviations* (Wiley, 1997).

[6] R. Chetrite and H. Touchette, Variational and optimal control representations of conditioned and driven processes, *Journal of Statistical Mechanics: Theory and Experiment* **2015**, P12001 (2015).

[7] R. L. Jack and P. Sollich, Effective interactions and large deviations in stochastic processes, *Eur. Phys. J: Special Topics* , 2351 (2015).

[8] A. Das and D. T. Limmer, Variational control forces for enhanced sampling of nonequilibrium molecular dynamics simulations, *J. Chem. Phys.* **151**, 244123 (2019).

[9] A. Das, D. C. Rose, J. P. Garrahan, and D. T. Limmer, Reinforcement learning of rare diffusive dynamics, *The Journal of Chemical Physics* **155**, 134105 (2021).

[10] E. R. Heller and D. T. Limmer, Evaluation of transition rates from nonequilibrium instantons, *Phys. Rev. Res.* **6**, 043110 (2024).

[11] M. Venturoli, E. Vanden-Eijnden, and G. Ciccotti, Kinetics of phase transitions in two dimensional Ising models studied with the string method, *J. Math. Chem.* **45**, 188 (2009).

[12] C. Moritz, A. Tröster, and C. Dellago, Interplay of fast and slow dynamics in rare transition pathways: The disk-to-slab transition in the 2d Ising model, *J. Chem. Phys.* **147**, 152714 (2017).

[13] K. Lum and D. Chandler, Phase Diagram and Free Energies of Vapor Films and Tubes for a Confined Fluid, *Int. J. Thermophys.* **19**, 845 (1998).

[14] D. Nicolaides and R. Evans, Monte Carlo study of phase transitions in a confined lattice gas, *Phys. Rev. B* **39**, 9336 (1989).

[15] A. Vishnyakov and A. V. Neimark, Nucleation of liquid bridges and bubbles in nanoscale capillaries, *J. Chem. Phys.* **119**, 9755 (2003).

[16] A. Luzar and K. Leung, Dynamics of capillary evaporation. I. Effect of morphology of hydrophobic surfaces, *J. Chem. Phys.* **113**, 5836 (2000).

[17] K. Leung and A. Luzar, Dynamics of capillary evaporation. II. Free energy barriers, *J. Chem. Phys.* **113**, 5845 (2000).

[18] R. Evans, Fluids adsorbed in narrow pores: phase equilibria and structure, *J. Phys.: Condens. Matter* **2**, 8989 (1990).

[19] A. Tröster and K. Binder, Positive Tolman Length in a Lattice Gas with Three-Body Interactions, *Phys. Rev. Lett.* **107**, 265701 (2011).

[20] A. Tröster, M. Oettel, B. Block, P. Virnau, and K. Binder, Numerical approaches to determine the interface tension of curved interfaces from free energy calculations, *J. Chem. Phys.* **136**, 064709 (2012).

[21] L. Yao and R. L. Jack, Interfacial and density fluctuations in a lattice model of motility-induced phase separation, *J. Chem. Phys.* **162**, 114902 (2025).

[22] R. J. Allen, D. Frenkel, and P. R. ten Wolde, Simulating rare events in equilibrium or nonequilibrium stochastic systems, *J. Chem. Phys.* **124**, 024102 (2006).

[23] R. J. Allen, D. Frenkel, and P. R. ten Wolde, Forward flux sampling-type schemes for simulating rare events: Efficiency analysis, *J. Chem. Phys.* **124** (2006).

[24] R. J. Allen, C. Valeriani, and P. R. ten Wolde, Forward flux sampling for rare event simulations, *J. Phys.: Condens. Matter* **21**, 463102 (2009).

[25] J. Bialké, J. T. Siebert, H. Löwen, and T. Speck, Negative Interfacial Tension in Phase-Separated Active Brownian Particles, *Phys. Rev. Lett.* **115**, 098301 (2015).

[26] A. Patch, D. M. Sussman, D. Yllanes, and M. C. Marchetti, Curvature-dependent tension and tangential flows at the interface of motility-induced phases, *Soft Matter* **14**, 7435 (2018).

[27] E. Tjhung, C. Nardini, and M. E. Cates, Cluster Phases and Bubbly Phase Separation in Active Fluids: Reversal of the Ostwald Process, *Phys. Rev. X* **8**, 031080 (2018).

[28] L. Langford and A. K. Omar, Theory of capillary tension and interfacial dynamics of motility-induced phases, *Phys. Rev. E* **110**, 054604 (2024).

[29] X.-q. Shi, G. Fausti, H. Chaté, C. Nardini, and A. Solon, Self-Organized Critical Coexistence Phase in Repulsive Active Particles, *Phys. Rev. Lett.* **125**, 168001 (2020).

[30] G. Fausti, M. E. Cates, and C. Nardini, Statistical properties of microphase and bubbly phase-separated active fluids, *Phys. Rev. E* **110**, L042103 (2024).

[31] G. Fausti, E. Tjhung, M. E. Cates, and C. Nardini, Capillary Interfacial Tension in Active Phase Separation, *Phys. Rev. Lett.* **127**, 068001 (2021).

[32] F. Turci and N. B. Wilding, Wetting Transition of Active Brownian Particles on a Thin Membrane, *Phys. Rev. Lett.* **127**, 238002 (2021).

[33] F. Turci, R. L. Jack, and N. B. Wilding, Partial and complete wetting of droplets of active Brownian particles, *Soft Matter* **20**, 2060 (2024).

[34] Y. Zhao, R. Zakine, A. Daerr, Y. Kafri, J. Tailleur,

and F. van Wijland, Active Young-Dupré Equation: How Self-organized Currents Stabilize Partial Wetting, arXiv:2405.20651 (2024).

[35] N. Grodzinski, R. L. Jack, and M. E. Cates, Hydrodynamic theory of wetting by active particles, arXiv:2506.14559 (2025).

[36] N. Grodzinski, R. L. Jack, and M. E. Cates, Spontaneous ratchet currents and transition dynamics in active wetting, arXiv:2512.08761. (2025).

[37] D. M. Hoyle and S. M. Fielding, Age-dependent modes of extensional necking instability in soft glassy materials, *Phys. Rev. Lett.* **114**, 158301 (2015).

[38] A. Moriel and E. Bouchbinder, Necking instabilities in elastoviscoplastic materials, *Phys. Rev. Materials* **2**, 073602 (2018).

[39] E. Y. Lin and R. A. Riggleman, Distinguishing failure modes in oligomeric polymer nanopillars, *Soft Matter* **15**, 6589 (2019).

[40] K. Thijssen, T. B. Liverpool, C. P. Royall, and R. L. Jack, Necking and failure of a particulate gel strand: signatures of yielding on different length scales, *Soft Matter* **19**, 7412 (2023).

[41] P. Guan, S. Lu, M. J. B. Spector, P. K. Valavala, and M. L. Falk, Cavitation in amorphous solids, *Phys. Rev. Lett.* **110**, 185502 (2013).

[42] I. Singh, R. Narasimhan, and U. Ramamurty, Cavitation-induced fracture causes nanocorrugations in brittle metallic glasses, *Phys. Rev. Lett.* **117**, 044302 (2016).

[43] R. Long, C.-Y. Hui, J. P. Gong, and E. Bouchbinder, The fracture of highly deformable soft materials: A tale of two length scales, *Ann. Rev. Cond. Matt. Phys.* **12**, 71 (2021).

[44] J. Mason, C. Erignoux, R. L. Jack, and M. Bruna, Exact hydrodynamics and onset of phase separation for an active exclusion process, *Proc. R. Soc. A.* **479**, 20230524 (2023).

[45] C. Maes, Local detailed balance, *SciPost Phys. Lect. Notes* , 032 (2021).

[46] D. T. Gillespie, Exact stochastic simulation of coupled chemical reactions, *J. Phys. Chem.* **81**, 2340 (1977).

[47] N. Masuda and C. L. Vestergaard, *Gillespie Algorithms for Stochastic Multiagent Dynamics in Populations and Networks* (Cambridge University Press, 2022).

[48] B. Peters, *Reaction Rate Theory and Rare Events Simulations* (Elsevier, 2017).

[49] K. Kawasaki, Diffusion Constants near the Critical Point for Time-Dependent Ising Models. I, *Phys. Rev.* **145**, 224 (1966).

[50] Y. Ben Dor, S. Ro, Y. Kafri, M. Kardar, and J. Tailleur, Disordered boundaries destroy bulk phase separation in scalar active matter, *Physical Review E* **105**, 044603 (2022).

[51] T. S. van Erp, Dynamical rare event simulation techniques for equilibrium and non-equilibrium systems, *Adv. Chem. Phys.* **151**, 37 (2012).

[52] X. K. Xi, D. Q. Zhao, M. X. Pan, W. H. Wang, Y. Wu, and J. J. Lewandowski, Fracture of brittle metallic glasses: Brittleness or plasticity, *Phys. Rev. Lett.* **94**, 125510 (2005).

[53] R. Wittkowski, A. Tiribocchi, J. Stenhammar, R. J. Allen, D. Marenduzzo, and M. E. Cates, Scalar ϕ^4 field theory for active-particle phase separation, *Nat. Comms.* **5**, 4351 (2014).

[54] M. E. Cates and C. Nardini, Classical Nucleation Theory for Active Fluid Phase Separation, *Phys. Rev. Lett.* **130**, 098203 (2023).

[55] J. S. Liu, *Monte Carlo Strategies in Scientific Computing*, Springer Series in Statistics (Springer, New York, 2004).